

S. Y. Tong M. A. Van Hove
K. Takayanagi X. D. Xie (Eds.)

The Structure of Surfaces III

Proceedings of the 3rd International Conference
on the Structure of Surfaces (ICSOS III)
Milwaukee, Wisconsin, USA, July 9–12, 1990

With 374 Figures

Springer-Verlag
Berlin Heidelberg New York
London Paris Tokyo
Hong Kong Barcelona
Budapest

Contents

Introduction	1
------------------------	---

Part I	Techniques
---------------	-------------------

I.1 Theory

Microscopic Origins of Stress on Semiconductor Surfaces By R.D. Meade and D. Vanderbilt (With 2 Figures)	4
Energy Density Calculations Applied to GaAs Polar Surfaces By N. Chetty and R.M. Martin (With 1 Figure)	9
First Principles Calculation of Lattice Relaxation at Low Index Surfaces of Ag and Cu By K.P. Bohnen, Th. Rodach, and K.M. Ho	16
Surface Diffusion of Al(110) By P. Stoltze and J.K. Nørskov (With 2 Figures)	19
Theory of Submonolayer Alkali-Metal Chemisorption By Dingsheng Wang, Kailai Chen, Shiwu Gao, Ruqian Wu, and Ning Wang (With 9 Figures)	24
Downward Funneling Model of Low-Temperature Epitaxial Growth: A Hybrid Molecular Dynamics–Monte Carlo Study By D.E. Sanders and J.W. Evans (With 4 Figures)	38
Mapping of Crystal Growth onto the 6-Vertex Model By C. Garrod, M. Kotrla, A.C. Levi, and M. Touzani (With 4 Figures) . .	44
Characterizing the Evolution of Non-equilibrium Structure During Adsorption By J.W. Evans (With 1 Figure)	49
Dependence of Cluster Diffusivity upon Cluster Structure By H.C. Kang, P.A. Thiel, and J.W. Evans (With 3 Figures)	55

Interaction of Heavy Rare-Gas Atoms with Metal Surfaces: A Model Based on the Effective Medium Theory By M. Karimi, D. Ila, I. Dalins, and G. Vidali	60
--	----

I.2 Angle-Resolved Electron Diffraction

Angular Diffraction Patterns of Photoelectrons and Auger Electrons from Single-Crystal Cu(111) By X.-D. Wang, Y. Chen, Z.-L. Han, S.Y. Tong, and B.P. Tonner (With 3 Figures)	65
Surface Termination of Binary Epitaxial Compounds by High Angular Resolution X-Ray Photoelectron Diffraction By S.A. Chambers (With 3 Figures)	72
Multiple-Scattering Effects in Auger Electron Diffraction and Photoelectron Diffraction: Theory and Applications By A.P. Kaduwela, D.J. Friedman, Y.J. Kim, T.T. Tran, G.S. Herman, C.S. Fadley, J.J. Rehr, J. Osterwalder, H.A. Aebischer, and A. Stuck (With 4 Figures)	77
Inelastic Photoelectron Diffraction By G.S. Herman, A.P. Kaduwela, T.T. Tran, Y.J. Kim, S. Lewis, and C.S. Fadley (With 2 Figures)	85
Electron Diffraction from Al(001) By J. Osterwalder, T. Greber, S. Hüfner, H.A. Aebischer, and L. Schlapbach (With 2 Figures)	91
Photoelectron Diffraction Patterns by Display-Type Spherical Mirror Analyzer By H. Daimon, Y. Tezuka, N. Kanada, A. Otaka, S.K. Lee, S. Ino, H. Namba, and H. Kuroda (With 5 Figures)	96
Energy-Angle Multidetector-Type Electron Spectrometer for X-Ray Photoelectron Diffraction Studies By S. Kanayama, S. Teramoto, M. Owari, and Y. Nihei (With 4 Figures)	102
3D Images of Surface Structure from Photoelectron Holography By J.J. Barton and L.J. Terminello (With 2 Figures)	107

I.3 Low-Energy Electron Diffraction

New Developments in the Theory of LEED By P.J. Rous (With 2 Figures)	118
Progress in Automatic Structure Refinement with LEED By W. Moritz, H. Over, G. Kleinle, and G. Ertl (With 3 Figures)	128

Application of Direct Methods in LEED: Multilayer Relaxation, Adsorption Sites and Adsorbate Induced Reconstruction By K. Heinz, W. Oed, and J.B. Pendry (With 1 Figure)	139
Real-Space Multiple Scattering Theory Calculations of LEED Intensities for Stepped Surfaces By X.-G. Zhang, P.J. Rous, J.M. MacLaren, A. Gonis, M.A. Van Hove, and G.A. Somorjai (With 3 Figures)	144
A Simple Scheme for LEED Intensity Calculations By R.F. Lin, P.M. Marcus, and F. Jona (With 2 Figures)	150
A Video-LEED System Based on a Personal Computer and Frame-Grabber By D.L. Adams, S.P. Andersen, and J. Buchhardt (With 3 Figures)	156
I.4 Other Electron-Based Methods	
One-Beam RHEED for Surface Structure Analysis By A. Ichimiya (With 3 Figures)	162
Direct Observation of Surface Structures by a High Resolution UHV-SEM By S. Ino, A. Endo, and H. Daimon (With 3 Figures)	168
High Resolution Electron Energy Loss Spectroscopy as a New Tool to Determine the Structure of a Surface Reconstructed System By J. Szeftel, J. Colin de Verdière, G.S. Dong, and D. Muller (With 3 Figures)	174
Auger Photoelectron Coincidence Spectroscopy of Cobalt By S.M. Thurgate (With 5 Figures)	179
I.5 Atomic and Molecular Scattering	
Exact Theory of One-Phonon Amplitudes in Diffractive Atom-Surface Scattering By M.E. Flatté	185
Metastable Spin-Polarized He as a Probe of Surface Magnetism on NiO(100) By A. Swan, W. Franzen, M. El-Batanouny, and K.M. Martini (With 3 Figures)	190
Scattering of O ₂ from the Ag(110) Surface By X.Y. Shen, K.Q. Zhang, and Y.L. Tan (With 2 Figures)	197
I.6 STM and AFM	
Imaging Adsorbates on Metals by Scanning Tunneling Microscopy By S. Chiang, D.D. Chambliss, V.M. Hallmark, R.J. Wilson, and Ch. Wöll (With 9 Figures)	204

Scanning Tunneling Microscopy of Organic Conductors By A. Kawazu, N. Ara, and M. Yoshimura (With 12 Figures)	214
Restructuring and Symmetry of Surfaces: $\sqrt{3} \times \sqrt{3}$ -Ag on Si(111)7 \times 7 By K. Takayanagi (With 9 Figures)	227
Atomic Resolution Imaging of Glycine Molecules on Graphite in Water By W.S. Yang, Wenjun Sun, Jianxun Mou, and Junjue Yan (With 4 Figures)	237
Theory of Atomic Force Microscopy on Elastic Surfaces By W. Zhong, G. Overney and D. Tománek (With 3 Figures)	243

Part II Clean Metals

II.1 Elemental Metals

Microscopic Kinetics of the (1 \times 2) Missing Row Reconstruction of the Au(110) Surface By L.D. Roelofs and E.I. Martir (With 2 Figures)	248
Surface Structural Analysis of the (1 \times 2) and (1 \times 3) Phases of Pt{110} by Time-of-Flight Scattering and Recoiling Spectrometry By F. Masson and J.W. Rabalais (With 5 Figures)	253
Analysis of the Reconstructed Ir{110} Surface from Time-of-Flight Scattering and Recoiling Spectrometry By M. Shi, H. Bu, and J.W. Rabalais (With 3 Figures)	259
Thermally Activated Defects on Crystal Surfaces By B. Salanon, H.J. Ernst, F. Fabre, L. Barbier, and J. Lapujoulade (With 3 Figures)	264
The Surface Barrier Structure of Metals from Barrier-Induced Surface States and Resonances By A.S. Christopoulos and M.N. Read (With 1 Figure)	271

II.2 Alloys

Anomalous Surface Phase Formation on Pt ₃ Sn(110) By A.N. Haner, P.N. Ross, and U. Bardi (With 3 Figures)	276
Surface Relaxation of Fe ₇₂ Cr ₂₈ (110) By D.J. O'Connor and C. Xu (With 2 Figures)	282
The Structure of CuPd(110)(2 \times 1): A Case of Underlayer Ordering By M. Lindroos, C.J. Barnes, M. Bowker, and D.A. King (With 3 Figures)	287
Effect of Segregation on Angular Distributions of Cu and Pt from a CuPt Alloy Sputtered by Low-Energy Ar Ions By L.-P. Zheng, R.-S. Li, M.-Y. Li, and W.-Z. Shen (With 1 Figure) . . .	293

Studies of Surface and Interface Structure of Ni ₃ Al Alloy by AP-FIM By D.G. Ren (With 7 Figures)	298
Simulation of the Fe ₈₀ B ₂₀ Metallic Glass Surface By W. Kowbel, P. Tlomag, and W.E. Brower, Jr. (With 2 Figures)	303

Part III Adsorption on Metals

III.1 Metallic Adsorption and Growth

Energetics in Structure Transformation of Ir Clusters and Atomic Reconstruction of Ir Surfaces By Chong-lin Chen and Tien T. Tsong (With 5 Figures)	312
Observations of Cluster Structures on fcc (111) By S.C. Wang and G. Ehrlich (With 7 Figures)	317
Structure of Metal Overlayers by Low Energy Alkali Ion Scattering: Cu/Ru(0001) and Sn/Pt(111) By S.H. Overbury, D.R. Mullins, M.T. Paffett, and B. Koel (With 4 Figures)	323
Growth and Structure of Ordered Thin Films of Cu on Pd{001} By H. Li, S.C. Wu, D. Tian, J. Quinn, Y.S. Li, F. Jona, and P.M. Marcus (With 3 Figures)	328
Electric and Magnetic Hyperfine Fields at Ni(111) Surfaces and Ni/In Interface Compound Formation By R. Platzner, X.L. Ding, R. Fink, G. Krausch, B. Luckscheiter, J. Voigt, U. Wöhrmann, and G. Schatz (With 4 Figures)	333
Structure and Surface Alloy Formation of the Fe(100)/Pt Overlayer System Studied with HEIS By G.W.R. Leibbrandt, R. van Wijk, and F.H.P.M. Habraken (With 4 Figures)	339
Initial Growth and Structure of Pt on Ni(100) By S. Deckers, W.F. van der Weg, and F.H.P.M. Habraken (With 3 Figures)	345
Structural Studies of Mercury Overlayers on Cu(001) by Atom Beam Scattering and LEED By Wei Li, J.-S. Lin, M. Karimi, C. Moses, P.A. Dowben, and G. Vidali (With 4 Figures)	350
Yb on Al(001): A Two-Dimensional Disordered System By T. Greber, J. Osterwalder, and L. Schlapbach (With 3 Figures)	355
Order-Disorder Transition of 6 ML Fe Films on the Cu(100) Surface By C. Stuhlmann, U. Beckers, J. Thomassen, M. Wuttig, H. Ibach, and G. Schmidt (With 3 Figures)	360

The Growth of Au on Ag(110): From Bilayer to Multilayer By P. Fenter and T. Gustafsson (With 4 Figures)	366
Structure of Au and Pt Films on Pd(110): Deposition Temperature and Coverage Dependent (1×2) and (1×3) Reconstructions By P.J. Schmitz, H.C. Kang, W.-Y. Leung, and P.A. Thiel (With 3 Figures)	372
Faceting Induced by Ultrathin Metal Films: Pt and Au on W(111) By K.-J. Song, C.Z. Dong, and T.E. Madey (With 3 Figures)	378
Core Level Photoemission for the Study of Metallic Interfaces and Two-Dimensional Compounds By J.N. Andersen, A. Nilsson, O. Björneholm, and N. Mårtensson (With 1 Figure)	383
Temperature Dependence of the Work Function of Alkali-Metal Atoms Adsorbed on a Metal Surface By T. Kato and M. Nakayama (With 6 Figures)	388
 III.2 Non-metallic Adsorption	
A LEED Study of the Clean and Hydrogen-Covered W(310)-(1×1) Surfaces By D.L. Adams and S.P. Andersen (With 3 Figures)	395
Coverage Dependent Hydrogen Induced Restructuring of Rh(110) By K. Heinz, W. Nichtl-Pecher, W. Oed, H. Landskron, M. Michl, and K. Müller (With 2 Figures)	401
Atomic Beam Diffraction Studies of the Ordered Hydrogen Chemisorption Phases on Rh(110) By G. Parschau, E. Kirsten, and K.H. Rieder (With 3 Figures)	406
Structural Studies of Highly Corrugated Systems with Atomic Beam Diffraction: Hydrogen-Chemisorption on Missing-Row Reconstructed Pt(110) and Ir(110) By E. Kirsten and K.H. Rieder (With 3 Figures)	411
Temperature and Coverage Dependence of the Structure and Dynamics of Hydrogen on Pd(111) By C.-H. Hsu, B.E. Larson, M. El-Batanouny, C.R. Willis, and K.M. Martini (With 3 Figures)	416
Hydrogen Titration Studies of fcc Cobalt Layers on Cu(001) By M.T. Kief, G.J. Mankey, and R.F. Willis (With 3 Figures)	422
Disordered Adsorption of O and S on Ni(100) Studied by Diffuse LEED By U. Starke, W. Oed, P. Bayer, F. Bothe, G. Fürst, P.L. de Andres, K. Heinz, and J.B. Pendry (With 3 Figures)	427

A Directed LEED Search for Many Structural Parameters: Substrate Relaxations and Buckling in Mo(100)- $c(2\times 2)$ -C and -S By P.J. Rous, D. Jentz, D.G. Kelly, R.Q. Hwang, M.A. Van Hove, and G.A. Somorjai (With 1 Figure)	432
Lattice Gas Models for Order–Disorder Behaviour of Oxygen on Ruthenium(001) By K. De’Bell, H. Pfnür, and P. Piercy (With 2 Figures)	437
Phase Separation of the O/W(110) $p(2\times 1)+p(2\times 2)$ System By M.C. Tringides (With 2 Figures)	442
STM Studies of the Initial Stage of Oxygen Interaction with Ni(100) By G. Wilhelmli, A. Brodde, D. Badt, H. Wengelnik, and H. Neddermeyer (With 3 Figures)	448
O ₂ Induced $(1\times 3)\rightarrow(1\times 1)$ Phase Change of an Ir{110} Surface from TOF-SARS By H. Bu, M. Shi, and J.W. Rabalais (With 4 Figures)	456
Oxygen Induced Reconstruction of Cu(110) and Cu(100) Studied by STM By F. Jensen, F. Besenbacher, E. Lægsgaard, and I. Stensgaard (With 4 Figures)	462
Geometrical Structure of Molecular Adsorbates from Core-Level Binding Energies By A. Nilsson, H. Antonsson, A. Sandell, and N. Mårtensson (With 3 Figures)	467
Lateral Surface Stark Effect in Chemisorbed Molecules: CO on Metal Surfaces By B. Gumhalter, K. Hermann, and K. Wandelt (With 2 Figures)	473

Part IV Clean Semiconductors

IV.1 Elemental Semiconductors

Deposition and Annealing of Silicon on Cleaved Silicon Surfaces Studied by Scanning Tunneling Microscopy By R.M. Feenstra and M.A. Lutz (With 3 Figures)	480
Simulation and STM Studies of Equilibrium Properties of Vicinal Surfaces By T.L. Einstein, N.C. Bartelt, J.L. Goldberg, X.-S. Wang, E.D. Williams, and B. Joós (With 3 Figures)	486
The Precipitation of Kinks on Stepped Si(111) Surfaces By Jian Wei, N.C. Bartelt, and E.D. Williams (With 4 Figures)	492

Disordering of the (3×1) Reconstruction of Si(113): Realization of the Chiral Three-State Potts Model By Y.-N. Yang, N.C. Bartelt, T.L. Einstein, R.L. Park, and E.D. Williams (With 3 Figures)	497
Current Effects on Clean Si(111) and (001) Surfaces Studied by Reflection Electron Microscopy By A. Yamanaka, N. Ohse, H. Kahata, and K. Yagi (With 6 Figures) . . .	502
Morphology and Electron States Along Clean Si(100) Vicinal Surfaces By M. Khial, J.-P. Lacharme, and C.A. Sébenne (With 2 Figures)	507
2×1 Reconstructions of Si(001) Interfaces: Dimer and Non-dimer Models Derived from Grazing X-Ray Diffraction Data By N. Jedrecy, N. Greiser, M. Sauvage-Simkin, R. Pinchaux, J. Massies, and V.H. Etgens (With 3 Figures)	512
Kinematic Low-Energy Electron Diffraction Study of the Atomic Structure of the Si(001) 2×1 Surface By R.G. Zhao, Jinfeng Jia, Yanfang Li, and W.S. Yang (With 3 Figures)	517
X-Ray Photoelectron Diffraction Study of a High-Temperature Surface Phase Transition on Ge(111) By T.T. Tran, D.J. Friedman, Y.J. Kim, G.A. Rizzi, and C.S. Fadley (With 3 Figures)	522
Surface Mosaic of Multi-Component Systems By V.L. Avgustimov, D.I. Bidnyk, L.A. Bystraya, and S.P. Kostenko (With 4 Figures)	527
IV.2 Compound Semiconductors	
Electron–Hole Counting Rule at III–V Surfaces: Applications to Surface Structure and Passivation By D.J. Chadi (With 4 Figures)	532
The Dimerization of the Reconstructed Clean and Chemisorbed (100) Surfaces of Si and SiC By B.I. Craig and P.V. Smith (With 1 Figure)	545
Towards an Understanding of the Composition of the Reconstructed α SiC(000 $\bar{1}$) Surface By P. Badziag, M.A. Van Hove, and G.A. Somorjai (With 2 Figures) . . .	550
Structure of the GaAs(-1-1-1) 2×2 and GaAs (-1-1-1) $\sqrt{19} \times \sqrt{19}$ Surfaces By R.D. Bringans, D.K. Biegelsen, L.-E. Swartz, and J.E. Northrup (With 5 Figures)	555

A New Reconstruction of the GaP($\bar{1}\bar{1}\bar{1}$) Surface By X.Y. Hou, X.K. Lu, P.H. Hao, X.M. Ding, P. Chen, and X. Wang (With 4 Figures)	560
Atomic Geometry of the CdS($11\bar{2}0$) Surface By A. Kahn and C.B. Duke (With 2 Figures)	566
Strain Relaxation in Metastable Cubic CdS Epilayers By D.W. Niles and H. Höchst (With 3 Figures)	570

Part V Adsorbates on Semiconductors

V.1 Metallic Adsorption

Overview of Metal/Semiconductor Interfaces By Xie Xide (With 5 Figures)	576
Scanning Tunneling Microscopy Investigation of the K/Si(100) 2×1 Stepped (4°) Surface By P. Soukiassian and J.A. Kubby (With 5 Figures)	584
Lead Adsorption on Ge(001) and Si(001) Studied by Core-Level Spectroscopy By K. Hricovini, G. Le Lay, A. Kahn, A. Taleb-Ibrahimi, and J.E. Bonnet (With 2 Figures)	589
Location of Ag in Si(111)-($\sqrt{3}\times\sqrt{3}$)R 30° -Ag from X-Ray Standing Waves By E. Vlieg, E. Fontes, and J.R. Patel (With 2 Figures)	595
Study of ($\sqrt{3}\times\sqrt{3}$)R 30° Ag on Si(111) by Photoelectron Diffraction By G.S. Herman, A.P. Kaduwela, D.J. Friedman, M. Yamada, E.L. Bullock, C.S. Fadley, Th. Lindner, D. Ricken, A.W. Robinson, and A.M. Bradshaw (With 4 Figures)	600
Electronic and Atomic Structure of the Cu/Si(111)-Quasi- 5×5 Overlayer By T.N. Rhodin and D.D. Chambliss (With 3 Figures)	606
Structures Formed by Co-deposition of Two Metals on Si(111) 7×7 Surfaces Studied by Reflection Electron Microscopy By I. Homma, Y. Tanishiro, and K. Yagi (With 6 Figures)	610
Catalytic Effect of Metals (Sn, Ag, and Pb) on Homoepitaxial Growth of Ge and Si By K. Fukutani, H. Daimon, and S. Ino (With 5 Figures)	615
REM and RHEED Studies of Lead Adsorption on Silicon (111) Surfaces By Y. Tanishiro, M. Fukuyama, and K. Yagi (With 5 Figures)	623

Electron Accumulation Near the α -Sn/CdTe(111) Interface Region? By I. Hernández-Calderón and H. Höchst (With 3 Figures)	628
V.2 Non-metallic Adsorption	
Successive Oxidation Stages of Adatoms on the Si(111)7 \times 7 Surface Observed with Scanning Tunneling Microscopy and Spectroscopy By J.P. Pelz and R.H. Koch (With 3 Figures)	633
Full Ab Initio Determination of the Structural Parameters of H on GaAs(110) By C.M. Bertoni, F. Finocchi, M. Buongiorno Nardelli, F. Bernardini, and E. Molinari (With 2 Figures)	639

Part VI Oxides

Observation of a Corrugated Structure for the TiO ₂ (100) 1 \times 3 Surface Reconstruction By P. Zschack (With 2 Figures)	646
Simultaneous Epitaxial Growth of Two Differently Oriented Ni Island Structures upon TiO ₂ (110) By Ming-Cheng Wu and P.J. Møller (With 5 Figures)	652
Characterization of (100) and (111) Surfaces of MgO by Reflection Electron Microscopy By M. Gajdardziska-Josifovska, P.A. Crozier, and J.M. Cowley (With 3 Figures)	660
MgO(100) Structural Investigation Using EELFS and EXFAS Techniques By M. De Crescenzi, N. Motta, F. Patella, A. Sgarlata, F. Arciprete, A. Balzarotti, M. Benfatto, and C.R. Natoli (With 6 Figures)	665
LEED Studies of Krypton and Nitrogen Monolayers on MgO Single Crystals By T. Angot and J. Suzanne (With 4 Figures)	671
Structural Analysis of a Thin CaO Layer Formed by Electron Bombardment Heating on CaF ₂ (111) by Means of Chemical-State Discriminated XPED By C. Akita, T. Tomioka, M. Owari, A. Mizuike, and Y. Nihei (With 3 Figures)	676
Index of Contributors	681

Progress in Automatic Structure Refinement with LEED

W. Moritz¹, H. Over², G. Kleinle², and G. Ertl²

¹Institut für Kristallographie und Mineralogie, Universität München,
Theresienstr. 41, W-8000 München 2, Fed. Rep. of Germany

²Fritz-Haber-Institut der Max-Planck-Gesellschaft,
Faradayweg 4-6, W-1000 Berlin 33, Fed. Rep. of Germany

It is demonstrated that conventional least squares optimisation techniques can be successfully used for automatic structure refinement with LEED. Examples are given for two adsorbate systems, H/Ni(110)-(1x2) and O/Ni(110)-(2x1) where rapid convergence is reached in a simultaneous optimisation of all structural parameters within the top three layers.

1. Introduction

The application of LEED as a standard technique for surface structure determination relies critically on its convenient use and its capability to solve complex structures. An automatic structure refinement technique, a clear recipe to localise the best fit model and a standardised criterion to judge the quality of the result would be most useful to make the method applicable by the non-specialist. Clearly, this situation has not yet been reached and, compared to X-ray diffraction, the method is still limited. Recent developments, however, show that considerable improvements are possible. The computational effort, which is still a limiting factor, can be reduced to a large extent [1-3]. Further improvements can be made introducing optimisation techniques into the structure analysis.

Several procedures have been proposed for an automatic structure refinement in which a minimisation of the conventionally used R-factors is obtained by gradient methods or search procedures [4-6]. The first approach had been proposed by Powell and de Carvalho [4], who applied a search procedure with an independent optimisation of each parameter. The method is generally applicable and does not require the calculation of derivatives. A more sophisticated method which allows the simulta-

neous refinement of all parameters has been recently proposed by Rous, Van Hove and Somorjai [6]. This method is a gradient method which, in the formulation used there, also requires R-factor calculations only and no derivatives. A different approach, somewhat related to optimisation methods is the direct method proposed by Pendry, Heinz and Oed [5] in which the deviation from a reference structure is determined in one step. The procedure can be iterated if the linear expansion from the reference structure is not sufficient. The combination with Tensor LEED techniques [1] makes this method very efficient.

We propose here an alternative approach which closely resembles the methods conventionally applied in x-ray crystallography [7,8]. Both methods are diffraction techniques and the structure is usually determined by fitting model calculations to experimental data. The only difference in the two techniques is given by the way the experimental and theoretical data are compared, and, of course, in X-ray diffraction, further methods are applicable which cannot be applied with LEED. Using X-rays a set of diffracted intensities is measured at constant wavelength, while with LEED full spectra are measured and fitted to theoretical curves. The fit is usually done by adjusting the position of maxima and minima in the spectra.

There is a-priori no obvious reason why the simple comparison of relative intensities, which works well in the case of X-rays, should not work in the case of LEED. It should be noted that the position of maxima and minima in the spectra is not directly used. Measuring the distance between experimental and calculated spectra by the linear or quadratic deviation has the advantage that well developed optimisation techniques can be used. With the conventional R-factors, such as defined by Zanazzi and Jona [9] and Pendry [10] the fit-function becomes fairly complicated. A simpler R-factor therefore seems to be advantageous and it has indeed been shown that an R-factor based on the mean square deviation is well applicable and leads to reliable results. A full description of this method and the optimisation procedure has been published recently [7,8]. We therefore give here a short review of the novel structure refinement technique and discuss some calculational improvements in detail.

2. Optimisation procedure

The R-factors used in X-ray crystallography are either the linear or the mean square deviation between observed and calculated intensities at a fixed energy. The analogous approach in LEED has been proposed previously as the I(g) method [11]. The shortcomings of that method are that a superstructure producing only weak extra spots, such as a hydrogen superstructure, cannot be well determined because the I(E) spectrum of the superstructure spot is not properly weighted. This problem can be overcome by evaluating each beam with a separate weight factor. The R-factor is defined for discrete energies and is given by

$$R_{DE} = \sum_g W_g \frac{\sum_i |J_{i,g}^{\text{ex}} - c_g J_{i,g}^{\text{th}}|}{\sum_i J_{i,g}^{\text{ex}}} ; \quad (1)$$

$$c_g = \sum_i J_{i,g}^{\text{ex}} / \sum_i J_{i,g}^{\text{th}} ; \quad W_g = n_g / \sum_g n_g . \quad (2)$$

n_g is the number of points per beam g. This R-factor can be compared with the usual R-factor in x-ray diffraction. The quantity which is actually minimised in the optimisation procedure is, however, the mean square deviation R_2 . R_{DE} is used for comparison with x-ray diffraction where the unweighted linear deviation is a standard R-factor.

To save computing time it is advantageous to choose a step width on the energy scale which is as large as possible. We have extensively tested which step width can be chosen without losing precision of the result. A step width up to 15 - 20 eV corresponding to about 10 - 15 data points per spectrum seems to be completely sufficient [9,10]. The upper limit of the step width appears to be set by the requirement that enough points per beam remain.

Having defined the fit-function an automatic minimisation procedure can be introduced. A very efficient method has been developed by Marquardt [12]. His method combines the advantages of the gradient method and of the expansion method. In the gradient method the steepest decent of the R-factor in the parameter space is determined from its partial derivatives with respect to

all variable parameters. The method works well far away from the minimum but converges only slowly near the minimum where the derivatives become very small. The expansion method, on the other hand, works well near the minimum and may lead to serious errors far away from the minimum.

In the expansion method a linear approximation of the intensity function is used

$$I^{th}(\underline{p}_0 + \Delta \underline{p}) = I^{th}(\underline{p}_0) + \sum_{j=1}^k \left[\frac{\partial I^{th}(\underline{p}_0)}{\partial p_j} \right] \Delta p_j + \dots \quad (3)$$

where $\underline{p}_0 = (p_1, \dots, p_k)$ denotes the set of structural parameters and I^{ex} , I^{th} are the normalized intensities. Eq. (3) is inserted into the minimum condition

$$\partial R / \partial p_j = 0, \quad (j=1, \dots, k) \quad (4)$$

leading to a set of linear equations

$$\sum_{i=1}^n \{ I_i^{ex} - I_i^{th}(\underline{p}_0) - \sum_{j=1}^k \frac{\partial I_i^{th}(\underline{p}_0)}{\partial p_j} \Delta p_j \} \cdot \frac{\partial I_i^{th}(\underline{p}_0)}{\partial p_m} = 0 \quad (5)$$

which is solved by matrix inversion

$$\Delta \underline{p} = \beta \cdot \alpha^{-1}, \quad (6)$$

$$\beta_m = \sum_{i=1}^n (I_i^{ex} - I_i^{th}(\underline{p}_0)) \frac{\partial I_i^{th}(\underline{p}_0)}{\partial p_m}, \quad (7)$$

$$\alpha_{jm} = \sum_{i=1}^n \left[\frac{\partial I_i^{th}(\underline{p}_0)}{\partial p_i} \cdot \frac{\partial I_i^{th}(\underline{p}_0)}{\partial p_m} \right]. \quad (8)$$

The method of Marquardt replaces α_{jm} by

$$\alpha'_{jm} = \alpha_{jm} (1 + \delta_{jm} \cdot \lambda) \quad (9)$$

δ_{jm} is the Kronecker symbol. If λ is large then the diagonal terms dominate and the result is similar to the gradient method, if λ is small the expansion method is recovered. λ is dynamically adjusted by

$$\lambda = c \sum_{i=1}^k \frac{\beta_i^2}{\alpha_{ii}} \left(\frac{1}{R_2} \right) \quad (10)$$

The speed of the optimisation can be influenced by the parameter c .

3. Calculation of derivatives

The calculational effort in the procedure described above increases linearly with the number of free parameters because the numerical calculation of each derivative requires an additional full dynamical calculation per parameter at all energies. This calculation could be done very efficiently by applying the Tensor LEED technique [1]. However, an approximate calculation of derivatives seemed to be easier to implement in the existing program and turns out to be quite efficient. A linear approximation in calculating derivatives can be used.

The layer scattering matrices are approximated by:

$$M_{gg'} = M_{gg'}(\mathbf{p}_0) + \sum_j \frac{\partial M_{gg'}(\mathbf{p}_0)}{\partial p_j} \Delta p_j + \dots \quad (11)$$

where $\partial M_{gg'}/\partial p_j$ can be obtained from a linear expansion of the inverse of the propagator matrix. The definition of the propagator matrix and the layer scattering matrices is given in ref. 13. In a linear expansion

$$\begin{aligned} [1-X(\mathbf{p}_0+\Delta\mathbf{p})]^{-1} &= [1-X(\mathbf{p}_0)]^{-1} + [1-X(\mathbf{p}_0)]^{-1} \cdot \\ &\quad [X(\mathbf{p}_0+\Delta\mathbf{p})-X(\mathbf{p}_0)] \cdot [1-X(\mathbf{p}_0)]^{-1} \end{aligned} \quad (12)$$

and only matrix multiplications are required. The inverse of $[1-X(\mathbf{p}_0)]$ has been already calculated for the reference structure and can be reused again. Next an approximate calculation of the lattice sum is desirable. The sum over scattered waves from all atoms in the layer within a limiting radius of about 10 - 15 interatomic distances requires a good part of the computing time and it is worth while considering simplifications. The lattice sum of scattering paths between planes ν and ν' is

given by [13]

$$F_{\ell,m}^{\nu\nu'} = \sum_P i^\ell h_\ell(|k| \cdot |P+p_\nu - p_{\nu'}|) \cdot Y_{\ell m}(\Omega_{P+p_\nu - p_{\nu'}}) e^{-ik(P+p_\nu - p_{\nu'})} \quad (13)$$

The spherical harmonics $Y_{\ell m}(\Omega_{P+p_\nu - p_{\nu'}})$ do not change much by increasing p_ν by Δp_ν and for the Hankel functions the asymptotic behaviour at large P can be used to calculate the derivatives for values $P > P_{\min}$. P_{\min} can be set to 3-4 interatomic distances without losing precision.

$$\frac{\partial h_\ell(z)}{\partial z} \approx i h_\ell(z) + e^{i(z - \ell\frac{\pi}{2} + \frac{\pi}{4})} \quad (14)$$

The lattice sum is therefore split up into two parts where only one part containing the near neighborhood of an atom needs to be recalculated. The minimum distance P_{\min} can be chosen to about three interatomic distances. The calculational effort for the lattice sum is reduced by a factor of 15 by this approximation. The comparison of an approximate calculation of derivatives with the full dynamic calculation is shown in fig. 1.

The approximate calculation of derivatives turns out to be completely sufficient for all types of parameters.

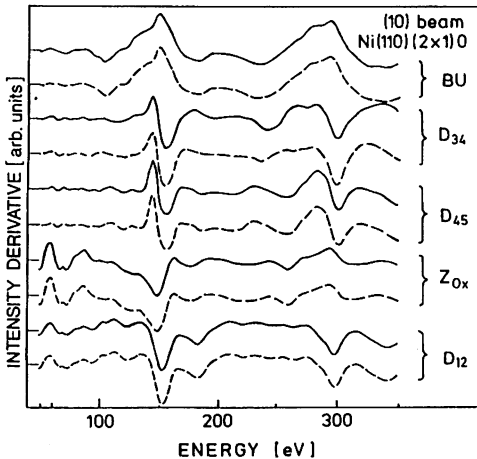


Fig.1. Comparison of approximate (dashed line) and full dynamical (solid line) calculation of derivatives. The structure parameters are displayed in fig. 2.

The increase of the speed of the calculation depends, however, on the number of variable parameters and the number of phase shifts used. In the examples shown below with 6 and 8 variable parameters a factor of 2.5 for the whole calculation is gained. Further improvements are possible. A linear expansion similar to that described in eq. (12) can be used for the matrices to be inverted in the layer doubling method.

4. Application to H/Ni(110)-(1x2) and O/Ni(110)-(2x1)

To illustrate the capability of the method the results of two adsorbate systems will be presented. Full structural results have been published recently [7,14,15], we present here only the results of the fit-procedure using the bulk values of Ni with a slight buckling in the third layer as start parameters.

The structure of the H/Ni(110)-(1x2) is shown in fig. 2; the hydrogen atoms are ignored in the calculation. The final structural parameters as well as the result of two calculations with different start parameters are given in table 1. The choice of the bulk structure as start parameter is not possible in this case. The bulk structure does not produce superstructure beams and the derivatives with respect to the superstructure parameters LS and BU vanish. The derivative vanishes because at a highly symmetry point two choices of the derivative are symmetrically equivalent. It is therefore necessary to shift at least one atom off its bulk lattice position.

A second example is O/Ni(110)-(2x1). The structural model is shown in fig. 3. Here 6 independent parameters within the top three layers had to be refined, assuming

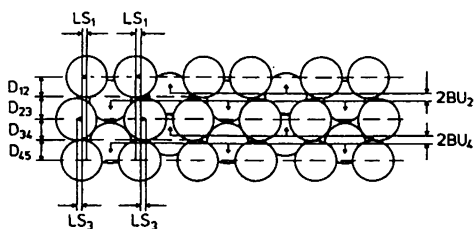


Fig. 2. Model of the (1x2) structure of H/Ni(110).
Hydrogen atoms are not shown.

Table 1. Result of a simultaneous fit of 8 structural parameters. The final structure was reached after 10 iterations, $R_{DE} = 0.3$

Parameter	Start Value	Final Value [Å]
D ₁₂	1.246	1.223
D ₂₃	1.246	1.331
D ₃₄	1.246	1.272
D ₄₅	1.246	1.220
LS ₁	0	0.30
LS ₃	0	0.12
BU ₂	0.1	0.25
BU ₄	0	0.02

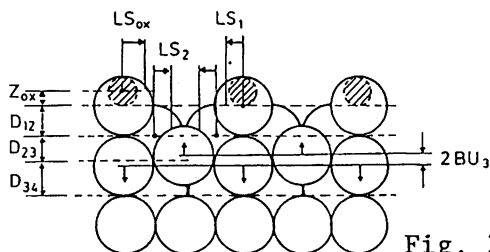


Fig. 3 Model of O/Ni(110)-(2x1)

Table 2. Result of a simultaneous fit of 6 parameters, the minimum R-factor was reached after 7 iterations, $R_{DE} = 0.24$

Parameter	Start Value	Final Value [Å]
Z _{ox}	0.3	0.224
D ₁₂	1.246	1.293
D ₂₃	1.246	1.246
LS ₂	0	0.011
BU ₄	0	0.052

that oxygen sits in the symmetric position. Results are shown in table 2. 15 eV steps were used in the energy range between 40 and 340 eV, corresponding to 106 data points in 8 I/V spectra.

In the above calculations oxygen was fixed in the symmetric site. A detailed study showed that a slight preference was found for an asymmetric site [14]. The search

for an asymmetric site was stimulated by a HREELS study [16] which showed an additional oxygen mode not compatible with the assumption of a symmetric oxygen position. This asymmetry has been neglected here, because it is felt that from the LEED data at normal incidence alone this asymmetry cannot be definitely concluded [14]. The influence of a lateral shift of the oxygen atom on the other structural parameters can be neglected.

5. Discussion

A central point in any optimisation scheme is of course the radius of convergence within which a minimum will be localised. That the minimum may be a local minimum has been already pointed out. Local minima can be avoided only by choosing start structures on a wide grid in the parameter space. The radius of convergence therefore determines the grid size which must be applied to exclude local minima. This same problem occurs, by the way, in the conventional R-factor analysis. The average distance between local minima in the R-factor hyperface may be estimated to be about 0.5 Å. This results from the simple consideration that with an average wavelength of 1.0 Å an interference maximum of backward and forward scattering between two atoms occurs again after a shift of 0.5 Å. It follows that roughly a deviation of 0.2 - 0.3 Å can be tolerated in the start parameters. This is a rough estimate, of course, and applies to parameters parallel to Δk . Smaller distances between local minima may also occur due to domain averaging [6].

To check the radius of convergence we performed several runs with different start values for two parameters in the O/Ni(110)-(2x1) structure, Z_{Ox} and D_{12} , keeping all other parameters at their optimum value. The results are shown in table 3.

It may be concluded that the radius of convergence is about 0.2 Å in agreement with the estimate considered above. In test runs with a simultaneous fit of all parameters the same radius of convergence was found which indicates that the parameters are only weakly correlated.

The convergence depends also on the parameter c in eq. 10, this has been chosen as 0.2 in the above examples. A larger value decreases the speed of the calcula-

Table 3 Check of the radius of convergence for two parameters.

	start	final	R _{DE}	No. of iterations
Z _{ox}	0.5	0.83	0.43	6
Z _{ox}	0.4	0.22	0.243	4
D ₁₂	1.5	1.58	0.73	1
D ₁₂	1.4	1.31	0.242	3

tion and has been found sometimes to increase the radius of convergence because the large steps in the beginning of the iteration process are damped.

Acknowledgement

Part of this work was financially supported by the Deutsche Forschungsgemeinschaft, SFB 338.

Literature

- [1] P.J. Rous, J.B. Pendry, D.K.Saldin, K. Heinz, K. Müller and N.Bickel, Phys. Rev. Letters 57 (1986) 2951.
- [2] W. Moritz, J. Phys. C17 (1984) 353.
- [3] J.B. Pendry and K. Heinz, Surf. Sci., in press.
- [4] P.G. Powell and V.E. de Carvalho, Surf. Sci. 187 (1987) 175
- [5] J.B. Pendry, K. Heinz and W. Oed, Proceedings of the 11th Intern Vac. Cong. (Colonge, 1989)
- [6] P. Rous, M.A. Van Hove and G.A. Somorjai, Surf. Sci. 226 (1990) 15, and this volume.
- [7] G. Kleinle, W. Moritz, D.L. Adams, and G. Ertl, Surf. Sci. 219 (1989) L637.
- [8] G. Kleinle, W. Moritz and G. Ertl, Surf. Sci. in press.
- [9] E. Zanazzi and F. Jona, Surf. Sci. 62 (1977) 61.
- [10] J.B. Pendry, J. Phys. C 13 (1980) 937.
- [11] a) L.J. Clarke, Surface Crystallography - An Introduction to Low Energy Electron Diffraction (Wiley Chichester, 1985).
b) L.J. Clarke, Vacuum 29 (1979) 405.

- [12] D.W. Marquardt, J. Soc. Indust. Appl. Math. 11 (1963) 431
- [13] J.B. Pendry, Low Energy Electron Diffraction, Academic press, London and New York 1974.
- [14] G. Kleinle, R.J. Behm, F. Jona, W. Moritz, J. Winterlin and G. Ertl, Surf. Sci. 225 (1990) 171.
- [15] E. Kleinle, V. Penka, R.J. Behm, G. Ertl and W. Moritz, Phys. Rev. Letters 58 (1987) 148.
- [16] B. Voigtländer, S. Lehwald and H. Ibach, Surf. Sci. 225 (1990) 162